nature materials

SUPPLEMENTARY INFORMATION
https://doi.org/10.1038/s41563-018-0242-y

In the format provided by the authors and unedited.

Double-lattice photonic-crystal resonators enabling high-brightness semiconductor lasers with symmetric narrow-divergence beams

Masahiro Yoshida[1], Menaka De Zoysa[1], Kenji Ishizaki[1], Yoshinori Tanaka[1], Masato Kawasaki[1,2], Ranko Hatsuda[1], Bongshik Song[1,3], John Gelleta[1] and Susumu Noda[1*]

[1]Department of Electronic Science and Engineering, Kyoto University, Kyoto, Japan. [2]Advanced Technology R&D Center, Mitsubishi Electric Corporation, Hyogo, Japan. [3]Department of Electrical and Computer Engineering, Sungkyunkwan University, Suwon, South Korea. *e-mail: snoda@kuee.kyoto-u.ac.jp

SUPPLEMENTARY INFORMATION

Double-Lattice Photonic-Crystal Resonators Enabling Semiconductor Lasers with High-Brightness and Symmetric Narrow-Divergence Beams

Masahiro Yoshida[1], Menaka De Zoysa[1], Kenji Ishizaki[1], Yoshinori Tanaka[1], Masato Kawasaki[1,2], Ranko Hatsuda[1], Bongshik Song[1,3], John Gelleta[1], and Susumu Noda[1]*

[1]Department of Electronic Science and Engineering, Kyoto University, Kyoto, 615-8510, Japan.

[2]Advanced Technology R&D Center, Mitsubishi Electric Corporation, Hyogo 661-8661, Japan.

[3]Department of Electrical and Computer Engineering, Sungkyunkwan University, Suwon 16419, South Korea.

*e-mail: snoda@kuee.kyoto-u.ac.jp

S1. Brightness of laser beams

The brightness B of a semiconductor laser is given by

$$B = \frac{P}{S \times \Omega}, \tag{S1}$$

where P, S, and Ω are the output power, emission area, and solid angle of the emitted beam, respectively[S1,S2]. According to Eq.(S1), higher brightness can be achieved by increasing the output power P while keeping the product of the emission area S and the beam divergence Ω as small as possible.

Generally, for a semiconductor laser with a single (lateral) mode, the output power P is proportional to the emission area S; namely, P is limited by the onset of catastrophic optical damage (COD), and increasing S raises the threshold for COD, and thus the limit on P, by reducing the optical power density. In addition, increasing S narrows the solid angle Ω of the emitted beam. Altogether, $P \propto S$ and $\Omega \propto 1/S$, so B in Eq.(S1) can be rewritten as follows.

$$B \propto \frac{S}{S \times 1/\mathrm{S}} \propto S\,. \tag{S2}$$

This expression shows that the brightness of the laser can be increased by widening the emission area, provided that the laser continues to operate in a single lateral mode.

However, widening the emission area usually entails the formation of additional, high-order lateral modes which widen the divergence angle[S3-S8]. For a laser with a rectangular emission area, when the laser operates in a high-order mode of order m in the x direction and order n in the y direction, the laser effectively operates as a combination of smaller emitters, each with an emission area $1/(m+1)(n+1)$ times smaller, and hence a divergence angle $(m+1)(n+1)$ times wider, than that of a single-mode laser. This widening of the divergence angle negatively impacts the brightness, as expressed by the following relation.

$$B \propto \frac{S}{(m+1)(n+1)}. \tag{S3}$$

Incidentally, the denominator of Eq.(S1) can be rewritten as $\mathrm{S} \times \Omega = \pi^2 \mathrm{BPP}^2$ by using beam quality (beam parameter product, BPP), and thus brightness $B = P/\pi^2\mathrm{BPP}^2$, where BPP is the product of the near-field width and the beam divergence angle. In the main text, B is calculated using the measured near-field width and beam divergence angle (inferred from the far-field width) estimated from the individual $1/e^2$ width, based on this relationship.

S2. 2D photonic band structure and optical coupling to form 2D broad-area resonance, and coupled-wave theory

Let us consider a single lattice shown in Fig.1b of the main text, where a single elliptical hole with a low dielectric constant inside a high-dielectric semiconductor is periodically arranged with a periodicity of a in the x and y directions. We define here the change of dielectric constant relative to the high-dielectric background as $\varepsilon(x,y)$. Owing to its periodicity, $\varepsilon(x,y)$ can be expressed as a Fourier expansion using reciprocal lattice vector $\mathbf{G}_{m,n} = \left(\frac{2\pi m}{a}, \frac{2\pi n}{a}\right)$ with integers m and n:

$$\varepsilon(x,y) = \sum\nolimits_{m,n} F_{m,n} \exp\left\{ \mathrm{j}\left(\frac{2\pi m}{a} x + \frac{2\pi n}{a} y \right) \right\}. \tag{S4}$$

Here, $F_{m,n}$ are Fourier coefficients, which can be derived from the original dielectric distribution $\varepsilon(x,y)$ as:

$$F_{m,n} = \frac{1}{a^2} \iint_{-a/2}^{a/2} \varepsilon(x,y) \exp\left\{ -\mathrm{j}\left(\frac{2\pi m}{a} x + \frac{2\pi n}{a} y \right) \right\} dxdy \,. \tag{S5}$$

The above dielectric distribution has a photonic band structure as shown in Fig.S1a, where the dispersion relationship for the transverse-electric (TE) modes are shown. We focus on the band edges of the Γ_2 point in this band structure, where four fundamental Bloch waves S_x, R_x, S_y and R_y (green arrows in Fig.S1b), with wave vectors (k_x, k_y) of ($-2\pi/a, 0$), ($2\pi/a, 0$), ($0, -2\pi/a$), and ($0, 2\pi/a$) propagating in the $\pm x$ and $\pm y$ directions, are coupled with each other to form 2D broad area resonance.

The optical coupling among four fundamental Bloch waves are induced by reciprocal lattice vectors $\mathbf{G}_{m,n} = \left(\frac{2\pi m}{a}, \frac{2\pi n}{a}\right)$ at strengths proportional to $F_{m,n}$. The direct 180° couplings from S_x to R_x and from R_x to S_x in the x direction are induced by $\mathbf{G}_{2,0}$ and $\mathbf{G}_{-2,0}$, respectively, and direct 180° couplings from S_y and R_y and from R_y and S_y in the y direction are induced by $\mathbf{G}_{0,2}$ and $\mathbf{G}_{0,-2}$, respectively. We note that 180° couplings can be also induced indirectly by a set of reciprocal lattice vectors via a higher-order Bloch wave, although their contribution is much smaller than those of direct couplings described above. For a photonic crystal with inversion symmetry along the $y=-x$ axis, the total strength of 180° coupling from S_x to R_x and from R_y to S_y (from R_x to S_x and from S_y to R_y) is given by coefficients κ_{1D+} (κ_{1D-}) (see Fig.S1c).

The orthogonal (or 90°) optical couplings among the fundamental waves, i.e., S_x and S_y, S_x and R_y, R_x and S_y, and R_x and R_y are also important to realize 2D resonance. Although these couplings seem to be achieved directly by the reciprocal vectors $\mathbf{G}_{\pm1,\mp1}$, $\mathbf{G}_{\pm1,\pm1}$, $\mathbf{G}_{\mp1,\mp1}$, and $\mathbf{G}_{\mp1,\pm1}$, respectively, they are in reality forbidden, as the inner product of the electromagnetic fields of two orthogonal Bloch waves is zero for TE-polarized light. However, indirect coupling by a set of reciprocal lattice vectors through a higher-order Bloch wave is possible (see Fig.S1b). For example, 90° coupling from S_x to S_y is induced by a set of reciprocal lattice vectors $\mathbf{G}_{m,n}$ and $\mathbf{G}_{-m+1,-n-1}$ through a higher-order Bloch wave with a wave vector of $[(-2\pi/a, 0)+\mathbf{G}_{m,n}]$, where m and n are arbitrary integers. Similarly, coupling from S_x to R_y is induced by $\mathbf{G}_{m,n}$ and $\mathbf{G}_{-m+1,-n+1}$, coupling from R_x to S_y is induced by $\mathbf{G}_{m,n}$ and $\mathbf{G}_{-m-1,-n-1}$, and coupling from R_x to R_y is induced by $\mathbf{G}_{m,n}$ and $\mathbf{G}_{-m-1,-n+1}$ through their respective higher-order Bloch waves. Couplings from S_y to S_x, from R_y to S_x, from S_y to R_x, and from R_y to R_x are also possible in similar fashion. The total indirect strength of 90° coupling from S_x to S_y and from R_y to R_x (from S_x to R_y and from S_y to R_x) is given by the coefficient κ_{2D+} (κ_{2D-}). Meanwhile, the strength of coupling in the reverse order (e.g., from S_y to S_x) is given by the complex conjugate of the corresponding coefficient. These couplings are summarized in Fig.S1d.

Comprehensive expressions for κ_{1D+}, κ_{1D-}, κ_{2D+}, and κ_{2D-} are given by Eq.(A15) in Ref.[S9]. Specifically, expressions for κ_{1D+} are given by row 1 column 2 and row 4 column 3 of Eq.(A15); expressions for κ_{1D-} are given by row 2 column 1 and row 3 column 4; expressions for κ_{2D+} are given by row 1 column 3 and row 4 column 2; and expressions for κ_{2D-} are given by row 1 column 4 and row 3 column 2. The calculated magnitudes of these coupling coefficients for a single-lattice photonic crystal and the double-lattice photonic crystals (structures I-III) in the main text are summarized in Fig.S2. Clearly, the 180° coupling strengths $|\kappa_{1D+}|$ and $|\kappa_{1D-}|$ are drastically reduced in structures I-III, because the mutual interaction between the two lattices weakens the direct couplings by $\mathbf{G}_{\pm 2,0}$ and $\mathbf{G}_{0,\pm 2}$. On the other hand, the 90° coupling strengths $|\kappa_{2D+}|=|\kappa_{2D+}^{*}|$ and $|\kappa_{2D-}|=|\kappa_{2D-}^{*}|$ are preserved across all photonic crystals.

Using the above coupling coefficients, we can calculate the lasing characteristics of the resonant band-edge modes. The following equations are derived using three-dimensional coupled-wave theory[S9-S11].

$$(\delta+i\frac{\alpha}{2})\begin{pmatrix} R_x \\ S_x \\ R_y \\ S_y \end{pmatrix}=\mathbf{C}\cdot\begin{pmatrix} R_x \\ S_x \\ R_y \\ S_y \end{pmatrix}+i\begin{pmatrix} \partial R_x/\partial x \\ -\partial S_x/\partial x \\ \partial R_y/\partial y \\ -\partial S_y/\partial y \end{pmatrix}, \tag{S6}$$

$$\mathbf{C}=\begin{pmatrix} \kappa_0 & \kappa_{1D+} & \kappa_{2D+} & \kappa_{2D-} \\ \kappa_{1D-} & \kappa_0 & \kappa_{2D-}^{*} & \kappa_{2D+}^{*} \\ \kappa_{2D+}^{*} & \kappa_{2D-} & \kappa_0 & \kappa_{1D-} \\ \kappa_{2D-}^{*} & \kappa_{2D+} & \kappa_{1D+} & \kappa_0 \end{pmatrix}. \tag{S7}$$

Here, $\mathbf{C}$ is a 4×4 matrix whose individual elements are the 180°-, 90°-, and self-coupling (κ_0) coefficients, δ is the frequency deviation from the Bragg condition, and α is the threshold gain. We note that α accounts for the total optical loss of the resonator. ($\alpha=\alpha_{rad}+\alpha_{edge}$, where α_{rad} is the vertical radiation and α_{edge} is the in-plane loss from the edges.) The equation is solved over a finite area using the staggered-grid finite-difference method[S11,S12]. Solutions of Eq.(S6) provide the lasing characteristics (e.g., frequency, threshold gain, and electric field distribution) of the resonant modes.

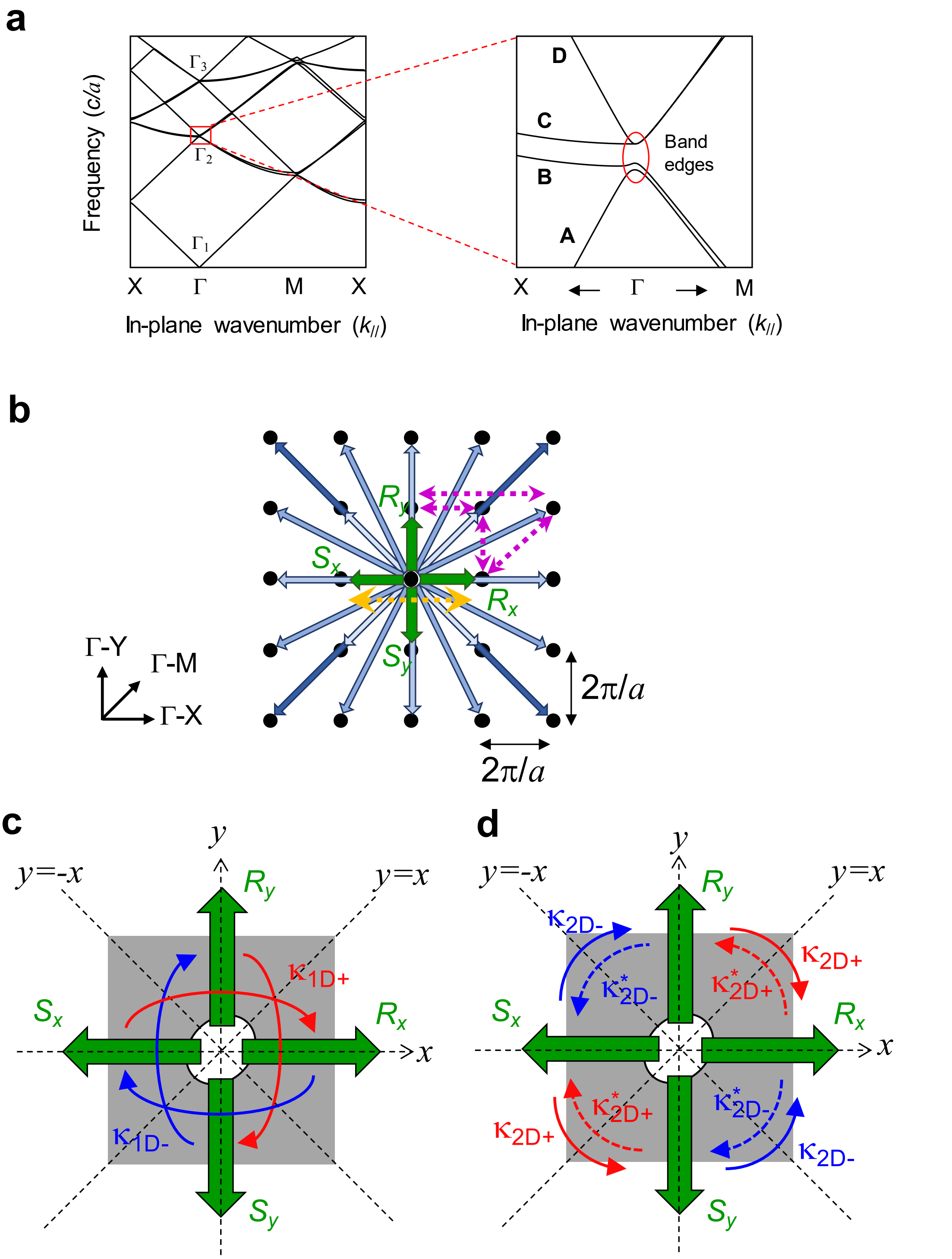

Supplementary Figure S1 | Photonic band structure and coupling diagram of a typical single-lattice photonic crystal. a, (Left) Band structure of a single-lattice photonic crystal. (Right) An enlarged image of this band structure around the Γ_2-point band edges, whose edges of bands A-D are circled in red. **b,** In-plane coupling diagram. The four basic waves are shown as green arrows. Higher-order waves are shown as arrows of progressively darker shades of blue color. The dashed yellow and purple arrows illustrate examples of 180° and 90° couplings, respectively. **c,** Schematic of 180° optical coupling. The red arrows indicate 180° coupling κ_{1D+} from basic wave S_x to R_x (R_y to S_y), and the blue arrows indicate 180° coupling κ_{1D-} from basic wave R_x to S_x (S_y to R_y). **d,** Schematic of 90° optical coupling. The solid red arrows indicate 90° coupling κ_{2D+} from S_x to S_y (R_y to R_x), and the solid blue arrows represent 90° coupling κ_{2D-} from S_x to R_y (S_y to R_x). The dashed red and blue arrows indicate 90° coupling in the reverse order, and are given by the complex conjugate of κ_{2D+} and κ_{2D-}.

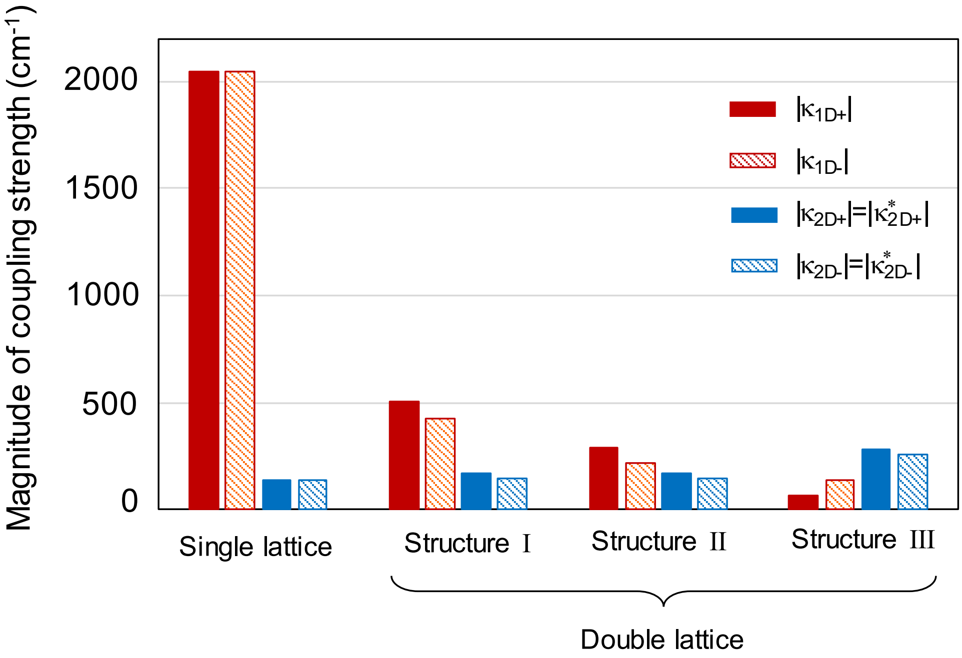

Supplementary Figure S2 | 180° and 90° coupling strengths of single-lattice and double-lattice photonic crystals. Shown are the magnitudes of 180° and 90° coupling strengths of double-lattice photonic crystal with structures I-III presented in Fig.2a in the main text. Those of a single-lattice photonic crystal of circular air holes with a similar air-hole size are also shown for comparison.

S3. Out-of-plane diffraction of double-lattice photonic-crystal resonators

We explain the effect of in-plane symmetry of the photonic-crystal air hole shape on out-of-plane diffraction which constitutes the surface emission, and then show how the shape can be tailored to enhance surface emission. Previous work has demonstrated that hole shapes with vertical and in-plane asymmetries are advantageous for enhancing the out-of-plane diffraction of a single-lattice photonic crystal resonator[S10,S13]. (It is worth noting that without such asymmetries the two lowest-threshold modes are in fact bound states in the continuum[S14] whose surface emission is forbidden.) The strength of surface emission depends on the degree of asymmetry. For example, for a double-lattice photonic crystal of circular air holes of identical size and depth, surface emission is zero. Figure S3a illustrates that this is a consequence of symmetry; namely, the electric field vectors of the light diffracted from the adjacent holes are equal in magnitude and opposite in phase, so they cancel out. This cancellation is abated with vertical and/or in-plane asymmetry. For example, if these two holes were to have different heights (i.e., vertical asymmetry), then the electric field distribution would be slightly shifted toward the taller hole, resulting in a difference in the electric field strength at each hole (see structure I and II in Fig.S3b). Alternatively, if the two holes were to have different shapes (i.e., in-plane asymmetry), then the degree of electric-field overlap at each hole would differ (see structure III in Fig.S3b). In either case, the electric field vectors of light diffracted from each hole no longer cancel, and surface emission is strengthened. The radiation constant of each structure in Fig.S3b is as follows: I: 30.1 cm^{-1}, II: 25.2 cm^{-1}, III: 22.6 cm^{-1}.

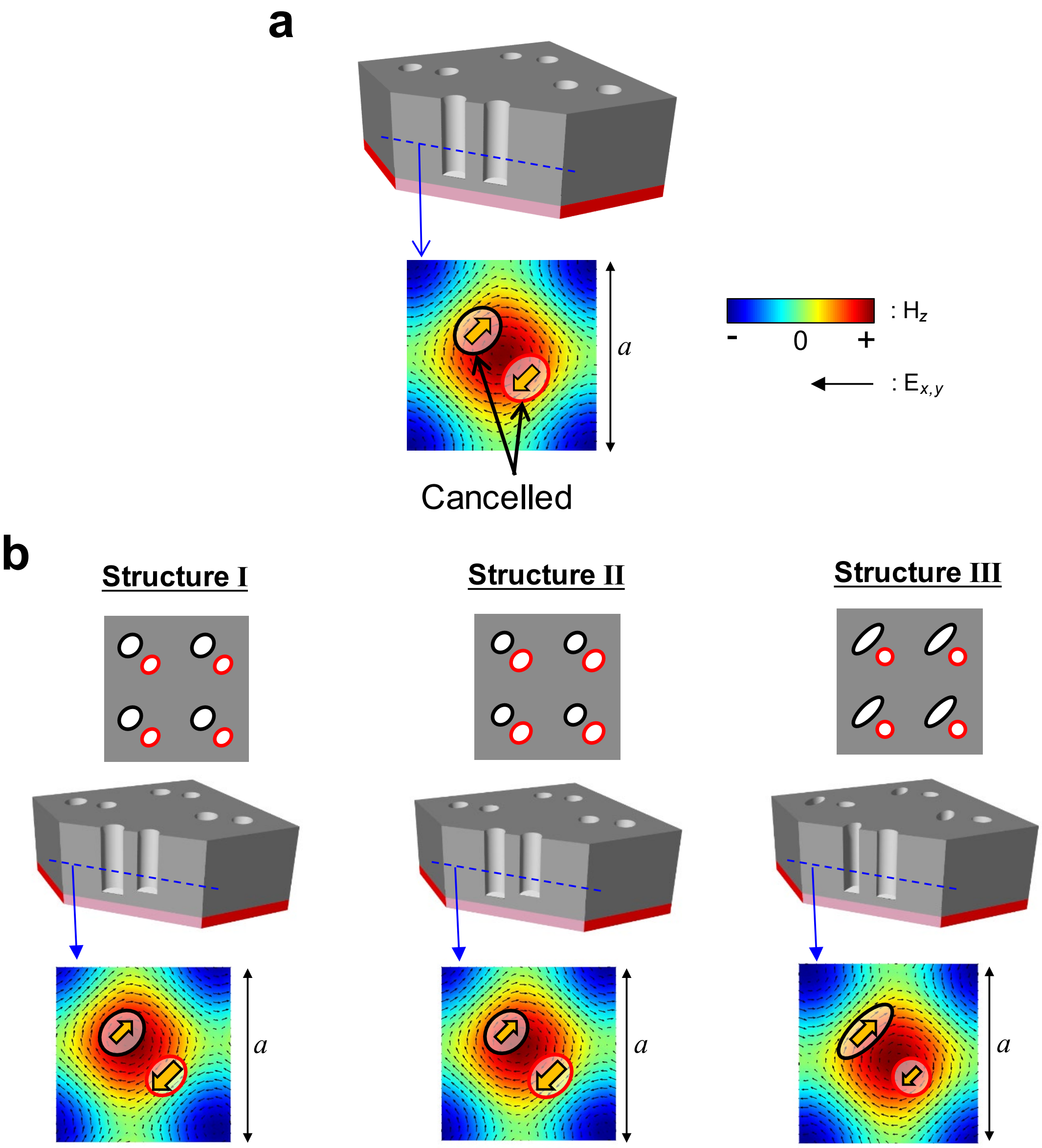

Supplementary Figure S3 | Out-of-plane diffraction in double-lattice photonic crystals. a, The electric field distribution within the unit cell of a double-lattice photonic crystal of circular air holes of identical size and depth. The electric field vectors (yellow arrows) of the light diffracted from the adjacent holes are equal in magnitude and opposite in phase, so they cancel out. As a result, surface emission is zero. **b,** The electric field distribution of structures I-III, which have vertical and/or in-plane asymmetry. In structures I-II, the electric field distribution is slightly shifted toward the taller hole. In structure III, the degree of electric-field overlap at each hole differs. In either case, the electric field vectors of light diffracted from each hole do not cancel out, and thus surface emission is strengthened.

S4. Surface morphology after MOVPE regrowth on the photonic crystal

Here, we evaluate the surface morphology after MOVPE regrowth on the photonic crystal structure. Fig.S4a shows an image of the surface after regrowth observed using a differential interference contrast microscope. The region surrounded by a black dashed line is the region where the regrowth occurred a top the photonic crystal structure fabricated by electron beam lithography and a dry etching process. Outside this region, regrowth occurred atop a flat surface. It can be seen that the regrown surface both within and outside of the photonic crystal region is flat, and its surface morphology homogeneous. In addition, we evaluated the surface roughness within the photonic crystal region following regrowth using an atomic force microscope (AFM). Fig.S4b shows a measured AFM image. A smooth surface with a root-mean-square (RMS) roughness of 0.31 nm was observed. This result revealed that the surface roughness was on the order of a monolayer (which is ~0.28 nm thick for GaAs).

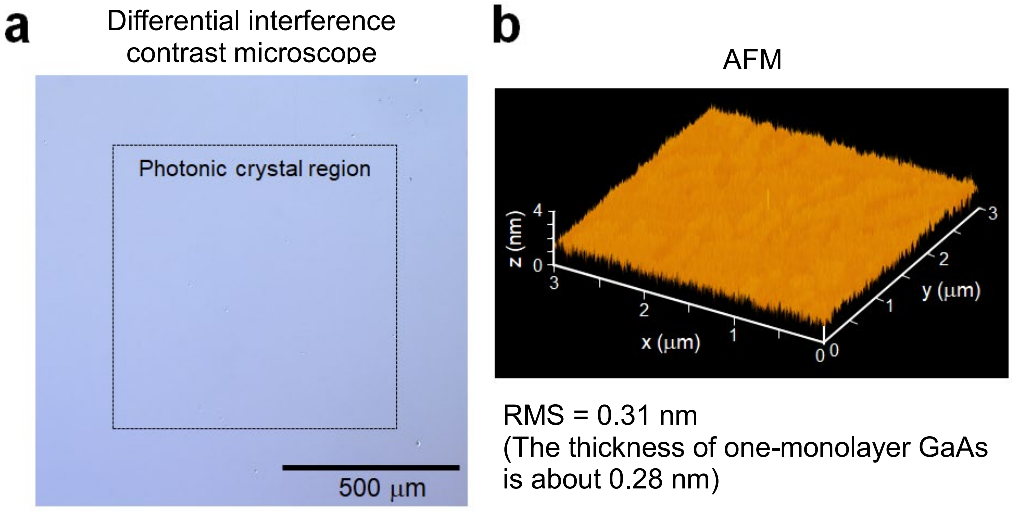

Supplementary Figure S4 | Surface morphology after the MOVPE regrowth on the photonic crystal. a, An image of the surface after regrowth observed using a differential interference contrast microscope. Regrowth in the region enclosed by the black dashed line occurred atop the photonic crystal structure. Regrowth outside of this region occurred atop a flat surface. **b,** An atomic force microscope (AFM) image within the photonic crystal region. A smooth surface with a root-mean-square (RMS) roughness of 0.31 nm was observed.

S5. Tuning the lattice separation of double-lattice photonic-crystal resonators

This section describes how we can tune the lattice separation of the photonic crystal resonator to achieve a balance of the coupling coefficients κ_{1D} and κ_{2D}, upon which the threshold gain difference $\Delta\alpha$ diverges as shown in Fig.5a of the main text. By adjusting the lattice separation d such that $d = 0.25a + \Delta d$, the contribution of direct 180° coupling, and thus the total magnitude and phase of κ_{1D}, can be controlled. On the other hand, κ_{2D}, which is determined not by direct coupling but by the sum of indirect couplings via higher-order waves, is relatively unaffected. Thus, for a realistic double-lattice photonic crystal structure, κ_{1D} can be balanced with κ_{2D} by introducing an adjustment of Δd from the nominal quarter-wavelength lattice separation.

We must note that, due to the asymmetry of the double-lattice photonic crystal, κ_{1D} and κ_{2D} are anisotropic (i.e., $\kappa_{1D+} \neq \kappa_{1D-}$, $\kappa_{2D+} \neq \kappa_{2D-}$), and thus the simultaneous cancellation of every 180° and 90° coupled wave at a single Δd is not guaranteed. Nevertheless, it is generally possible to obtain the cancellation of at least one pair of 180° and 90° coupled waves. As an example, we show in Figs.S5a and S5b the magnitudes and phases, respectively, of $\kappa_{1D\pm}$ and $\kappa_{2D\pm}$ as functions of Δd for structure IV in the main text. From Δd~0.010a to Δd~0.016a, κ_{1D+} and κ_{2D+} are similar in magnitude and differ by around π in phase. Figure S5c shows $\Delta\alpha$ as a function of Δd for structure IV whose $L = 1000\,\mu$m. At around $\Delta d = 0.012a$, κ_{1D+} and κ_{2D+} are balanced such that a wide $\Delta\alpha$ of over 15 cm^{-1} is obtained. If we can design some double-lattice resonator that balances not only κ_{1D+} and κ_{2D+}, but all combinations of $\kappa_{1D\pm}$ and $\kappa_{2D\pm}$, then $\Delta\alpha$ would diverge as in Fig.5a of the main text, and single-mode lasing with no limitation on resonator size would be realized.

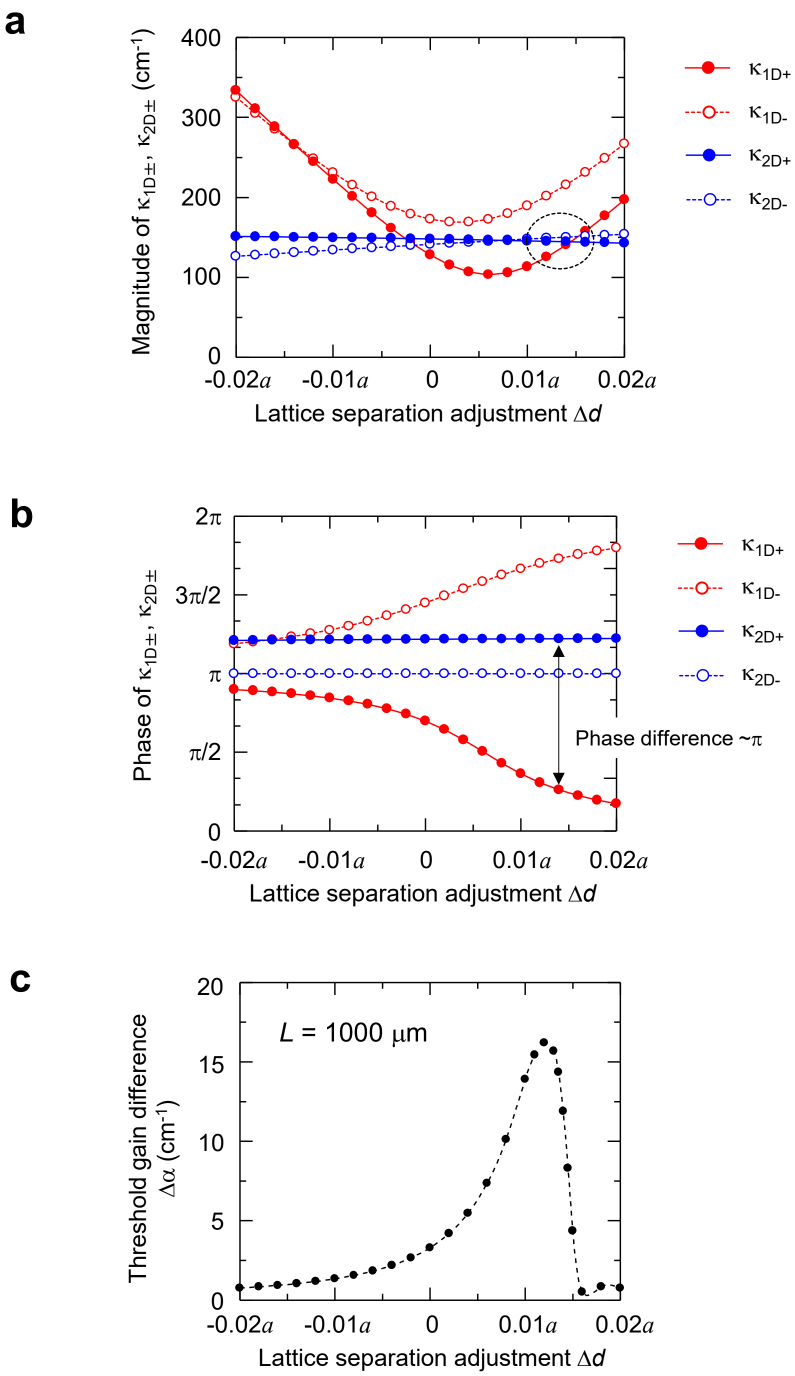

Supplementary Figure S5 | Effect of tuning the lattice separation of the double-lattice photonic crystals. The **a** magnitude and **b** phase of coupling coefficients κ_{1D+}, κ_{1D-}, κ_{2D+}, and κ_{2D-} as functions of the lattice separation adjustment Δd (where the total lattice separation $d = 0.25a + \Delta d$). A double-lattice photonic crystal defined as structure IV in the main text is considered. By tuning the lattice separation (i.e., when $d = 0.25a + \Delta d$), the strength of direct 180° coupling, and thus the total magnitude and phase of $\kappa_{1D\pm}$, can be controlled. On the other hand, $\kappa_{2D\pm}$, which are determined by the sum of coupling via many higher-order waves, are relatively unaffected. From Δd~0.010a to Δd~0.016a, κ_{1D+} and κ_{2D+} are similar in magnitude and differ by around π in phase. **c,** The threshold gain difference $\Delta\alpha$ as a function of the lattice separation adjustment Δd when the resonator diameter L is 1000 μm. A large $\Delta\alpha$ is obtained at around $\Delta d = 0.012a$ as a result of the balancing of κ_{1D+} and κ_{2D+}.

References

S1. Ross, T. S. & Latham, W. P. Appropriate measures and consistent standard for high energy laser beam quality. *J. Directed Energy* **2,** 22–58 (2006).

S2. Shukla, P., Lawrence, J. & Zhang, Y. Understanding laser beam brightness: a review and new prospective in material processing. *Opt. Laser Technol.* **75,** 40–51 (2015).

S3. Siegman, A. E. New developments in laser resonators. *Proc. SPIE* 1224, 2–14 (1990).

S4. Siegman, A. E. Defining, measuring, and optimizing laser beam quality. *Proc. SPIE* 1868, 2–12 (1993).

S5. Wenzel, H. *et al.* Theoretical and experimental analysis of the lateral modes of high-power broad-area lasers. *Proc. Numerical Simulation of Optoelectronic Devices (NUSOD)*, 143–144 (2011).

S6. Crump, P. et al. Experimental and theoretical analysis of the dominant lateral waveguiding mechanism in 975 nm high power broad area diode lasers. *Semicond. Sci. Technol.* **27,** 045001 (2012).

S7. Winterfeldt, M., Crump, P., Wenzel, H., Erbert, G. & Tränkle, G. Experimental investigation of factors limiting slow axis beam quality in 9xx nm high power broad area diode lasers. *J. Appl. Phys.* **116,** 063103 (2014).

S8. Chang-Hasnain, C. J et al. Transverse mode characteristics of vertical cavity surface-emitting lasers. *Appl. Phys. Lett.* **57,** 218–220 (1990).

S9. Liang, Y., Peng, C., Sakai, K., Iwahashi, S. & Noda, S. Three-dimensional coupled-wave model for square-lattice photonic crystal lasers with transverse electric polarization: A general approach. *Phys. Rev. B* **84,** 195119 (2011).

S10. Peng, C., Liang, Y., Sakai, K., Iwahashi, S. & Noda, S. Coupled-wave analysis for photonic-crystal surface-emitting lasers on air holes with arbitrary sidewalls. *Opt. Express* **19,** 24672–24686 (2011).

S11. Liang, Y., Peng, C., Sakai, K., Iwahashi, S. & Noda, S. Three-dimensional coupled-wave analysis for square-lattice photonic-crystal lasers with transverse electric polarization: Finite-size effects. *Opt. Express* **20,** 15945–15961 (2012).

S12. Sheen, D. H., Tuncay, K., Baag, C. E., & Ortoleva, P. J. Parallel implementation of a velocity-stress staggered-grid finite-difference method for 2-D poroelastic wave propagation. Computers and Geosciences **32,** 1182-1191 (2006).

S13. Hirose, K. *et al.* Watt-class high-power, high-beam-quality photonic crystal lasers. *Nature Photon.* **8,** 406–411 (2014).

S14. Hsu, C. W., Zhen, B., Stone, A. D., Joannopoulos, J. D., & Soljacic, M. Bound states in the continuum. *Nature Reviews Materials* **1**, 16048 (2016).